Clays and Clay Minerals, Vol. 51, No. 4, 457–472, 2003.

CHEMISTRY OF Mg SMECTITES IN LACUSTRINE SEDIMENTS FROM THE VICALVARO SEPIOLITE DEPOSIT, MADRID NEOGENE BASIN (SPAIN)

JAIME CUEVAS[1,*], RAQUEL VIGIL DE LA VILLA[1], SUSANA RAMIREZ[1,2], SABINE PETIT[2], ALAIN MEUNIER[2] AND SANTIAGO LEGUEY[1]

[1] Departamento de Química Agrícola, Geología y Geoquímica, Facultad de Ciencias, Universidad Autónona de Madrid. Cantoblanco s/n 28049 Madrid, Spain

[2] UMR 6532 CNRS, Universite de Poitiers, 40, Avenue du Recteur Pineau, 86022 Poitiers Cedex, France

Abstract—The chemical and structural properties of Mg smectites in the Vicálvaro sepiolite deposit have been studied in detail. The characterization was performed on different size-fractions of selected smectitic samples (5–2 μm; 2–1 μm; 1–0.5 μm; <0.5 μm and <0.1 μm). The chemical compositions of individual particles (5–1 μm) and of bulk undifferentiated fine fractions (1–<0.1 μm) were determined by energy dispersive spectroscopy-scanning electron microscopy and interpreted with the aid of X-ray diffraction (XRD) and infrared spectroscopy (IR) methods. The XRD and IR data demonstrate that all of the Mg smectite materials studied are mainly composed of a complex mixture of stevensite, saponite and mica-type minerals. Although the presence or absence of saponite cannot be confirmed absolutely, stevensite is a significant component of these Mg smectites. This is proven by the calculated layer charge reduction after the Hofmann-Klemen effect. The results are in close agreement with the suggested mechanism of topotactic overgrowth of stevensite on pre-existing phyllosilicate templates. This characterizes clay diagenesis in saline-lake systems.

Key Words—Fe-rich Dioctahedral Micas, Lacustrine Mg Clays, Saponite, Stevensite, Trioctahedral Smectites, Vicálvaro Sepiolite Deposit, Spain.

INTRODUCTION

Magnesium smectite beds form a significant part of the lacustrine sediments from the Madrid Neogene Basin, often related to the well known sepiolite deposits (Jones and Galán, 1988). Several authors have characterized different trioctahedral smectite-group minerals in this area, mainly saponite, stevensite or interstratified kerolite-stevensite (Galán *et al.*, 1986; Martin de Vidales *et al.*, 1988, 1991; Ordoñez *et al.*, 1991; Cuevas *et al.*, 1993; De Santiago *et al.*, 2000).

The formation of authigenic trioctahedral Mg smectites is facilitated by precipitation on pre-existing 2:1 phyllosilicate layer substrata according to Jones (1986). This process seems to proceed better in highly saline and alkaline environments (Darragi and Tardy, 1987; Hay *et al.*, 1991). This authigenic mechanism is in agreement with the predominance of multiphase mixtures rather than true solid-solutions belonging to the smectite group minerals (Vali *et al.*, 1993; Petit *et al.*, 1992).

The Vicálvaro deposit offers a good opportunity to study the diagenetic processes affecting lacustrine environments. Smectitic materials are found in significant quantities and as virtually monomineral beds (Ramirez *et al.*, 1996). This fact has allowed the characterization of saponitic and stevensite-type clays, based on bulk chemical analysis (Leguey *et al.* 1995). These materials generally showed higher Mg and lower K and Al contents than other chemical compositions determined in Mg smectites of similar lacustrine environments (Hay *et al.*, 1991; Jones, 1986 or Banfield *et al.*, 1991). The composition of some of these Mg smectites can easily be explained by addition of Mg silicate (stevensite or kerolite) layers to the pre-existing minerals of the dioctahedral phyllosilicate group (illite, beidellite). In contrast, some of the Vicálvaro and Madrid Basin saponitic clays are closer to the trioctahedral end-member (Galán *et al.*, 1986; Cuevas *et al.*, 1993). A problem arises as to whether Mg smectites of saponitic composition and sedimentary (lacustrine) origin can be considered as di-trioctahedral mixtures or true saponites. The main objective of this work is to elucidate the crystallochemical nature of Mg smectites in the Vicálvaro deposit and to relate present smectite compositions to pre-existing sheet-silicate materials.

GEOLOGICAL SITUATION

The distribution of mineralogical, chemical and microstructural features of the Vicálvaro deposit (Leguey *et al.*, 1995) showed the following sequence of materials from the centre to the periphery of the lacustrine area: Mg smectites; massive sepiolite; sepiolitic calcretes; silcretes and arkosic sepiolites (Figure 1).

Detrital Al-dioctahedral smectites (mainly montmorillonite), illite and kaolinite, predominate in the periphery of the lake environment. These minerals are often associated with calcite and silica crusts. In the

* E-mail address of corresponding author:
Jaime.Cuevas@uam.es
DOI: 10.1346/CCMN.2003.0510413

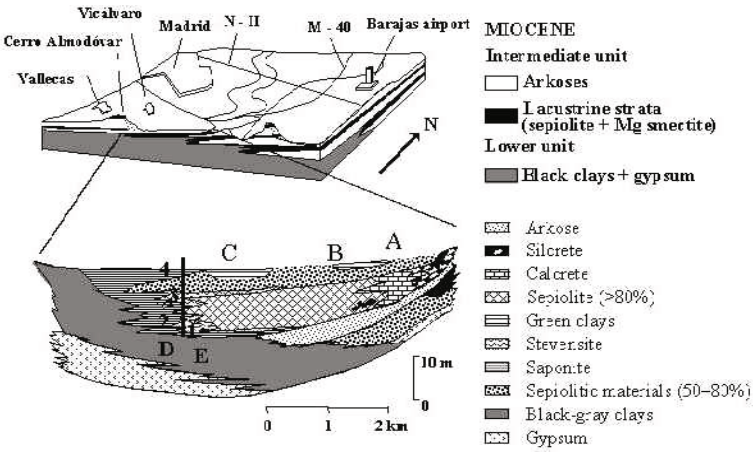

Figure 1. Lithology and geological setting of the Vicálvaro sepiolite deposit. Idealized sketch of the spatial distribution of lacustrine materials.

central-bottom areas, a similar assembly of dioctahedral phyllosilicates is mixed with gypsum, magnesite, dolomite and organic debris. These dioctahedral phyllosilicates are supposed to be the principal silicate reactants in the saline lake system.

The Mg smectite zone shows a vertical zonation with alternating saponitic and stevensitic compositions (Ramirez *et al.*, 1996). Zeolite (heulandite) is also found near the contact with the arkosic strata which are located above the lacustrine sedimentation episodes (Cuevas *et al.*, 1995). Two sepiolite beds can be distinguished in the vertical sequence. The upper sepiolite bed is interpreted as having originated from Mg-rich waters concentrated during desiccation periods of vertic horizons (paleosols) and is usually mixed with carbonates and Mg smectite. The lower bed is thicker. This massive bed of >80% sepiolite results from an alteration of Mg smectites by regional groundwater as suggested for the Amargosa sepiolitic deposit (Khoury *et al.*, 1982).

MATERIALS AND METHODS

Lithology and sample selection

The samples used in this study were chosen from among 80 studied during a previous and thorough characterization of four vertical sections in the Vicálvaro sepiolite deposit (Leguey *et al.*, 1995). Six samples from the center of the lacustrine area were selected for detailed study in the present work (Figure 1a, samples 1, 2, 3, 4, E and D). Samples 1, 2, 3 and 4 belong to a 15 m section containing a bed of high-grade sepiolite that is mined in the deposit. Hereafter these samples are referred to as lacustrine clays. They are of a whitish to pale gray color (lower sequence, samples 1 and 2) and a pale brown color (upper sequence, samples 3 and 4). According to the chemical analyses in previous works (Leguey *et al.*, 1995), samples 2 and 4 are considered to be saponitic smectite while samples 1 and 3 are more stevensitic. Samples D and E come from a test borehole below the mined sepiolitic section. These are clays representative of the basal strata of the lake deposit. Sample D is a dark green clay that frequently lies intercalated with detrital arkosic materials representing the transition between lutitic arkoses and the lacustrine sepiolite-smectite complex. Clay sample E is dark gray in color (black-gray clays in Figure 1) and shows gypsum traces (<5%) and significant organic carbon of ~2%. Samples D and E are referred to here as transitional and basal clays, respectively.

Mineralogy and chemical concentration of some elements of the lacustrine clays are represented in Figure 2. The sepiolite levels alternate with Mg smectite. The smectite is more or less mixed with illite, quartz and feldspar detrital minerals. These detrital beds are relatively enriched in Al_2O_3, K_2O and Fe_2O_3 as major elements and Zn^{2+} and Ba^{2+} as trace elements. The lowest sepiolite bed is located under a dolomitic layer. However, calcite is the main carbonate accompanying the clay materials upwards in the section. At the top of the sequence, the irregular contact zone between fine-grained arkoses and the smectitic materials contains zeolites and is enriched in Sr^{2+} and Ba^{2+}.

The Mg smectite/sepiolite materials in the lower sequence of the lacustrine clay section have high F contents (>1%), which decrease in the upper sequence. On the other hand, Li concentrations are relatively high (300–600 ppm) when Mg smectites predominate across the complete sequence. The F and Li contents, although important, are not high enough for hectorite, according to the formulae of Ames *et al.* (1958). The structural formula derived from the bulk chemical analysis of sample 1, Leguey *et al.* (1995), which is virtually composed of smectite, has been calculated including F and Li: $(Ca_{0.18}Na_{0.08}K_{0.10})(Mg_{5.34}Li_{0.08}Al_{0.15}Fe^{3+}_{0.09}Ti_{0.01})Si_{7.94}Al_{0.06}O_{20}(OH)_{3.47}F_{0.53}$.

https://doi.org/10.1346/CCMN.2003.0510413 Published online by Cambridge University Press

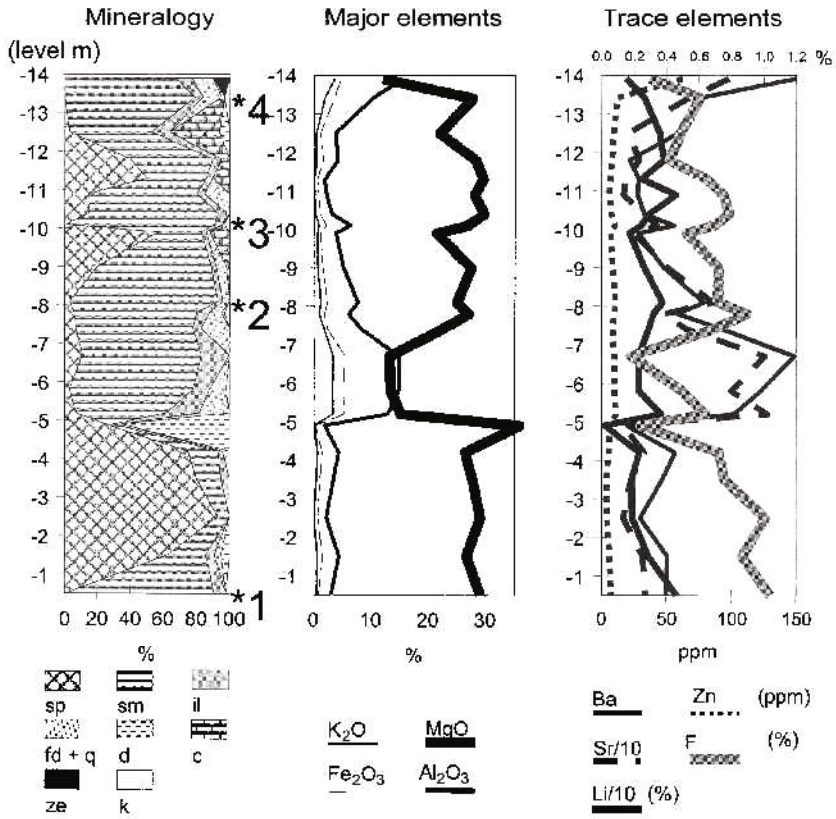

Figure 2. Mineralogy and geochemistry of the Vicálvaro sepiolite deposit. Mineralogical and chemical evolution of a vertical section in the central area of the lacustrine system (Figure 1).

The mineralogical and chemical compositions and some physicochemical properties of the selected samples have been compiled from works by Leguey *et al.* (1995) and Ramirez *et al.* (1996) (Tables 1 and 2). Sepiolite is virtually absent from these samples. Samples 1, 2, 3 and 4 are mainly composed of smectite while in samples D and E, the smectite is mixed with illite and kaolinite. Ca^{2+} predominates in the exchange complex of lacustrine clays (1 to 4) while Mg^{2+} is the main cation in the exchange complex of transitional and basal clays (samples D and E). Values of cation exchange capacity (CEC) and external surface are related to the amount of smectite. However, the high specific surface area measured in some of the Mg smectite specimens is associated with their stevensitic character, a fact that has previously been documented in similar clays (Cuevas *et al.*, 1993; Ramirez *et al.*, 1996; De Santiago *et al.*, 2000). Table 3 shows the chemical composition of the <0.5 μm Ca-homoionized fractions of smectites in the Madrid Basin: A, B, C, D, E, 1, 2, 3 and 4 from the Vicálvaro deposit (Figure 1) and A-II and B-I from the Cerro del Aguila deposit. Data from the A, B, 1, 2, 3, 4; E, D samples; and from the A-II and

Table 1. Mineralogical composition, CEC, chemical composition of the exchange complex and external surface (S_{ext}) of selected samples at the Vicálvaro deposit. All data are compiled from Ramírez *et al.* (1996) except CEC and S_{ext}. Mineralogical composition is semiquantitative (±5%).

Sample	Mineralogical composition (wt.%)[1]								CEC[2]	Ca^{2+}	Mg^{2+}	Na^{+}	K^{+}	S_{ext}[3]
	s	sp	m	k	q	f	c/d	gy	cmol/kg	% in exchange complex				m^2/g
4	76	–	13	–	6	5	tr	–	70	64	32	2	2	122
3	>95	–	tr	–	<5	tr	–	–	69	80	17	2	1	266
2	88	tr	8	–	<5	tr	–	–	49	59	36	2	3	237
D	58	–	31	5	<5	<5	–	–	26	42	56	1	1	86
E	35	–	22	18	13	7	<5	tr	11	23	73	3	1	26

[1] s: smectite; sp: sepiolite; m: hydrous mica or illite; k: kaolinite; q: quartz; f: feldspars; c/d: calcite/dolomite; gy: gypsum
[2] CEC determined using the Co(II) sulfate method (Rhodes and Brown, 1994)
[3] external surface determined using the N_2-BET method (Brunauer *et al.*, 1938)

https://doi.org/10.1346/CCMN.2003.0510413 Published online by Cambridge University Press

Table 2. Bulk chemical analyses of selected samples at the Vicálvaro deposit.

Sample	SiO_2	Al_2O_3	Fe_2O_3	TiO_2	MgO	CaO	K_2O	Na_2O	LOI	Sum	F^-	Li^+	Ba^{2+}	Sr^{2+}	Zn^{2+}
	%										ppm				
4	47.73	8.13	2.83	0.28	17.37	1.30	1.58	0.53	20.1	99.9	6080	332	75	122	67
3	50.01	2.52	0.85	0.12	23.29	0.96	0.27	0.20	21.7	99.9	7970	369	33	77	33
2	50.14	6.35	1.96	0.29	20.51	1.29	1.10	0.40	17.8	99.8	7175	472	79	108	86
1	49.36	2.34	0.72	0.15	22.27	1.06	0.48	0.25	23.3	99.9	10424	580	50	75	34
D	42.51	14.77	5.29	0.66	14.39	0.71	3.51	0.28	17.5	99.6	2135	132	105	n.d.	35
E	46.24	19.31	7.10	0.66	6.18	1.13	4.61	0.28	14.2	99.7	2065	230	208	n.d.	134

Data taken from Leguey *et al.* (1995)
LOI: loss on ignition

B-I samples were taken from the studies of Leguey *et al.* (1995), Ramirez *et al.* (1996) and Cuevas *et al.* (1993), respectively. The atomic distribution within a unit-cell of 44 negative charges is calculated from the chemical analysis (Table 3). The presence of large amounts of K^+ in the structure and its virtual absence in the exchangeable cations (Table 1) means that K^+ is retained in illite-type layers.

Methods

The six selected samples were dispersed in distilled water by continuous mechanical agitation with alternating cycles of ultrasonic treatment. Four fractions were separated by sedimentation and centrifugation procedures: 2–5 μm; 1–2 μm; 1–0.5 μm and <0.5 μm. These fractions were dried and crushed gently in an agate mortar. Powder samples were deposited on an adhesive film disc of graphite. The powders were analyzed by scanning electron microscopy (SEM) with an energy-dispersive X-ray spectrometer (EDS). The EDS measurements were calibrated using an internal standard, phlogopite (mica-Mg, CRPG standard), that fits the composition of analyzed samples closely.

Table 3. Chemical composition (wt.%) and atomic distribution within a unit-cell of 44 negative charge of the <0.5 μm Ca-homoionized fractions from smectitic samples in the Madrid Basin.

Sample	SiO_2	Al_2O_3	Fe_2O_3	TiO_2	MgO	CaO	K_2O	LOI	Sum
A*	52.30	15.71	5.57	0.32	4.31	2.33	1.45	17.9	99.89
B*	48.66	17.76	5.20	0.25	3.83	2.31	0.94	21.0	99.95
C*	49.46	6.16	2.02	0.12	17.95	1.42	0.64	22.1	99.87
D**	45.22	10.62	5.77	0.26	15.23	2.24	2.34	18.2	99.88
E**	46.07	22.29	7.07	0.36	3.76	1.46	4.17	14.7	99.88
1**	54.11	1.68	0.57	0.04	25.73	1.64	0.17	16.0	99.94
2**	49.90	5.20	1.41	0.08	22.07	2.17	0.44	18.7	99.97
3**	52.63	2.06	0.77	0.03	25.04	1.78	0.15	17.5	99.96
4**	49.20	6.63	2.36	0.10	20.95	2.36	0.76	17.4	99.76
A-II***	47.71	5.52	2.13	0.19	21.82	2.42	0.28	19.6	99.67
B-I***	48.21	7.09	3.13	0.26	20.28	2.43	0.66	17.7	99.76

Sample	Atomic distribution within a unit-cell of 44 negative charge
A*	$(Ca^{2+}_{0.37}K_{0.27})(Mg_{0.95}Al_{2.45}Fe^{3+}_{0.62}Ti_{0.04})\ (Al_{0.28}Si_{7.72})O_{20}(OH)_4$
B*	$(Ca^{2+}_{0.38}K_{0.18})(Mg_{0.87}Al_{2.65}Fe^{3+}_{0.60}Ti_{0.03})(Al_{0.55}Si_{7.45})O_{20}(OH)_4$
C*	$(Ca^{2+}_{0.24}K_{0.13})(Mg_{4.18}Al_{0.85}Fe^{3+}_{0.24}Ti_{0.01})(Al_{0.28}Si_{7.72})O_{20}(OH)_4$
D**	$(Ca^{2+}_{0.37}K_{0.46})(Mg_{3.50}Al_{0.90}Fe^{3+}_{0.67}Ti_{0.03})(Al_{1.03}Si_{6.97})O_{20}(OH)_4$
E**	$(Ca^{2+}_{0.23}K_{0.78})(Mg_{0.82}Al_{2.62}Fe^{3+}_{0.78}Ti_{0.04})(Al_{1.24}Si_{6.76})O_{20}(OH)_4$
1**	$(Ca^{2+}_{0.25}K_{0.03})(Mg_{5.55}Al_{0.12}Fe^{3+}_{0.06}Ti_{0.00})(Al_{0.17}Si_{7.83})O_{20}(OH)_4$
2**	$(Ca^{2+}_{0.35}K_{0.08})(Mg_{4.95}Al_{0.43}Fe^{3+}_{0.16}Ti_{0.01})(Al_{0.49}Si_{7.51})O_{20}(OH)_4$
3**	$(Ca^{2+}_{0.28}K_{0.03})(Mg_{5.51}Al_{0.12}Fe^{3+}_{0.08}Ti_{0.00})(Al_{0.24}Si_{7.76})O_{20}(OH)_4$
4**	$(Ca^{2+}_{0.38}K_{0.14})(Mg_{4.67}Al_{0.52}Fe^{3+}_{0.27}Ti_{0.01})(Al_{0.65}Si_{7.35})O_{20}(OH)_4$
A-II***	$(Ca^{2+}_{0.40}K_{0.05})(Mg_{5.00}Al_{0.33}Fe^{3+}_{0.25}Ti_{0.02})(Al_{0.67}Si_{7.33})O_{20}(OH)_4$
B-I***	$(Ca^{2+}_{0.39}K_{0.13})(Mg_{4.55}Al_{0.52}Fe^{3+}_{0.35}Ti_{0.03})(Al_{0.74}Si_{7.26})O_{20}(OH)_4$

* Vicálvaro deposit (from Leguey *et al.*,1995)
** Selected samples of this work (from Leguey *et al.*, 1995 and Ramirez *et al.*, 1996)
*** 'Cerro del Aguila' deposit (from Cuevas *et al.*, 1993)

https://doi.org/10.1346/CCMN.2003.0510413 Published online by Cambridge University Press

In the 5–2 μm and 2–1 μm size-fractions, individual particles were analyzed, preferentially on laminar clean surfaces, avoiding as far as possible the effects of some superposed spots of altered material or filling defects in the mica-type platelets. The 1–0.5 μm and <0.5 μm size-fractions were analyzed by selecting several zones along the mounted powder sample. Analyses were performed using a spot size of 100 nm and 50 s exposure (until 6000 counts s^{-1} were received). A separate analysis was performed in <0.5 μm Ca^{2+}-homoionized samples by X-ray fluorescence (XRF).

The <0.1 μm size-fraction was also obtained by centrifugation using a Beckman J2-21 centrifuge equipped with the JCF-Z continuous flow rotor in order to perform a detailed characterization by XRD and Fourier transform infrared spectroscopy (FTIR). The XRD diagrams, from powder and oriented ethylene glycol aggregates, were acquired using a SIEMENS KRISTALLOFLEX diffractometer (CuKα radiation) with a D-500 goniometer equipped with an EDS detector device. The deconvolution of XRD peaks has been performed using the commercial software Microsoft-

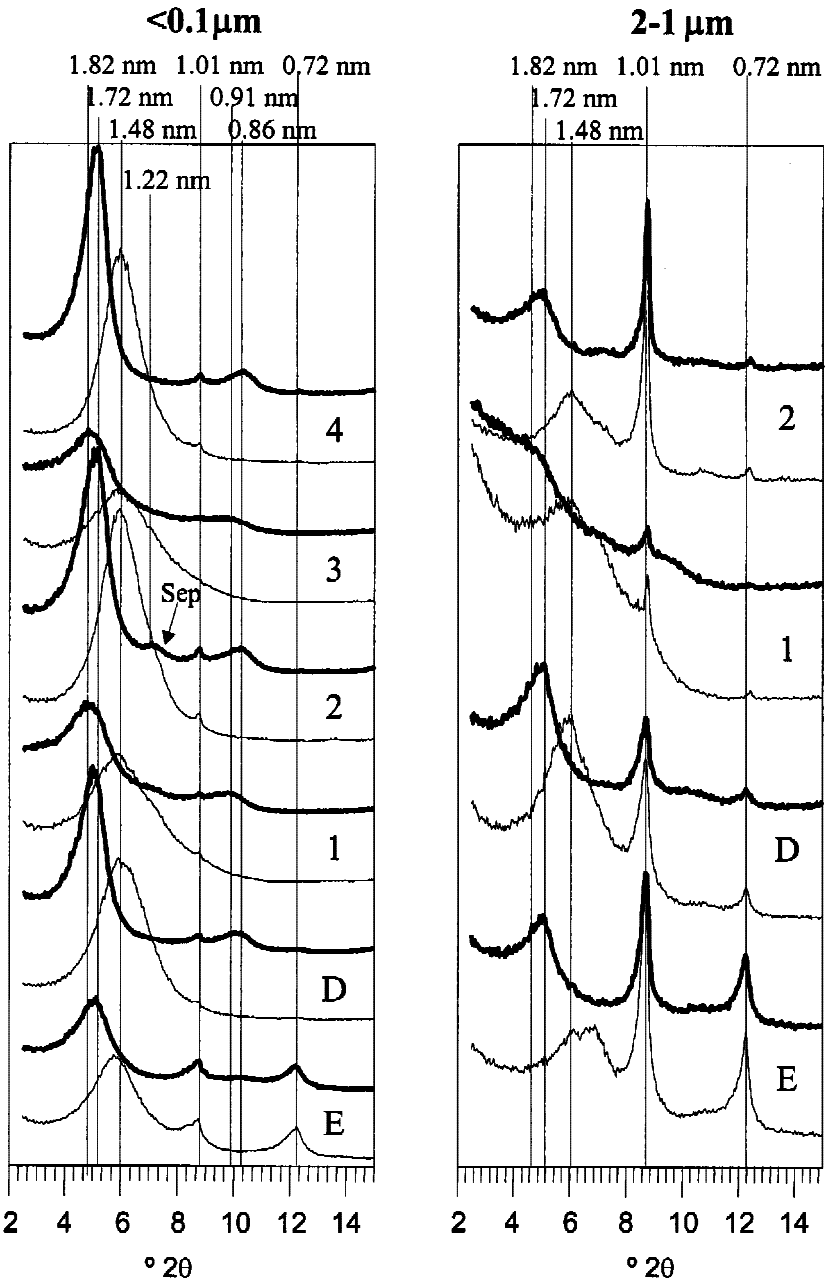

Figure 3. XRD patterns of the first- and second-order basal reflections of air-dried (thin line) and ethylene glycol-solvated oriented mounts (thick line) in the coarse (2–1 μm) and fine (<0.1 μm) fractions from the selected samples (Figure 1).

https://doi.org/10.1346/CCMN.2003.0510413 Published online by Cambridge University Press

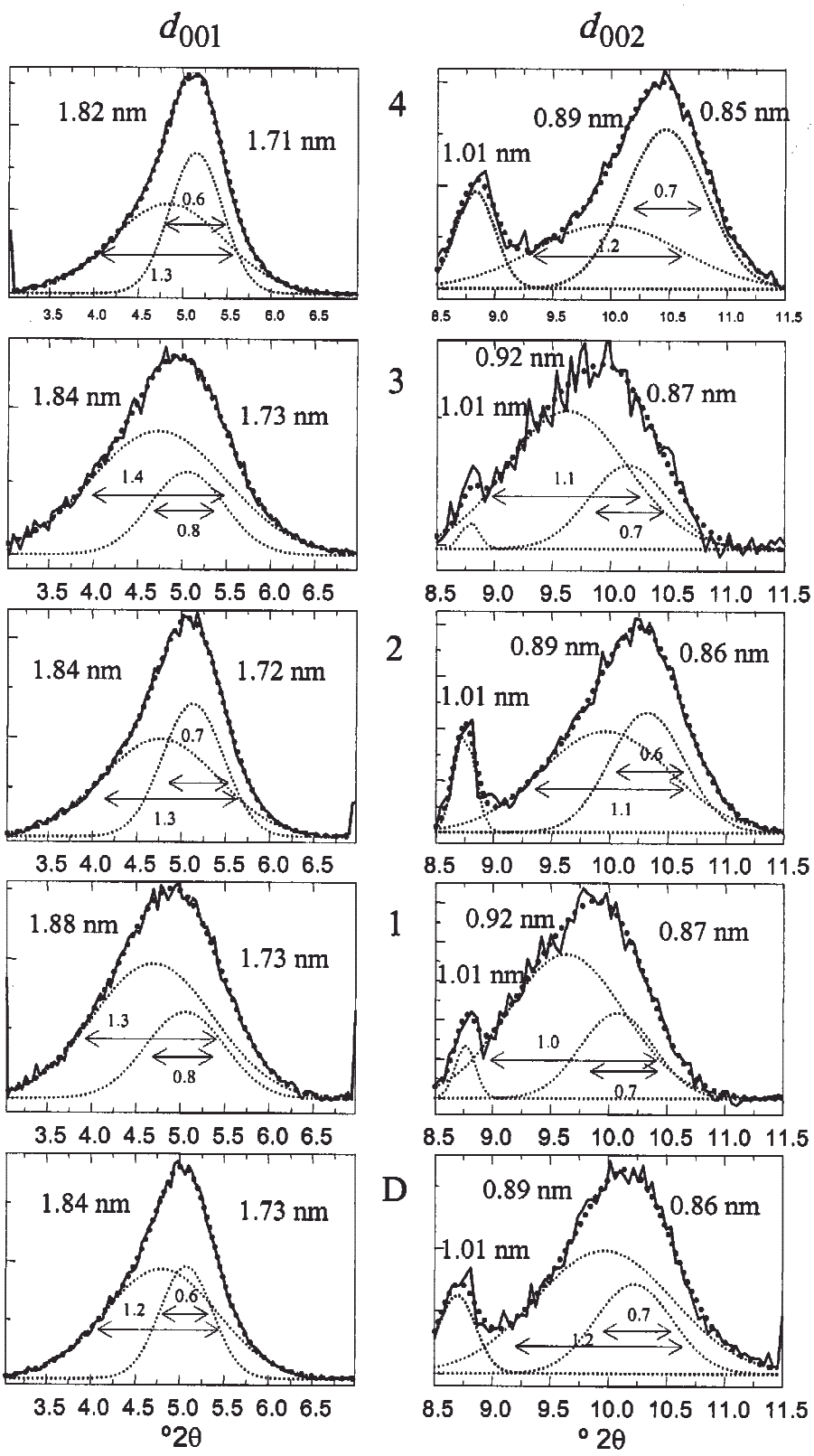

Figure 4. XRD pattern deconvolution for the first- and second-order basal reflections of ethylene glycol-solvated <0.1 μm fraction from the selected samples. FWHH data are presented within the deconvoluted peaks.

https://doi.org/10.1346/CCMN.2003.0510413 Published online by Cambridge University Press

Origin®. Gaussian functions were combined to reproduce the raw XRD profile.

The FTIR was performed on KBr disks prepared by compression of 3 mg of sample with 300 mg of KBr. The method of measuring the normalized intensity of the IR band assigned to the ammonium fundamental ν_4 mode of NH_4-exchanged clays before and after Li fixation (Hofmann and Klemen treatment) was used to estimate the layer-charge distribution of <0.1 μm smectite clays (Petit *et al.*, 1998, 1999).

RESULTS

XRD characterization

Figure 3 shows the XRD patterns of air-dried and ethylene glycol solvated oriented samples. The 2–1 μm fraction patterns confirm the detrital character of this fraction as long as sharp peaks of illite or mica-type minerals are significant. In addition, kaolinite is observed in small amounts, both in lacustrine (samples 1 and 2, in Figure 3) or in transitional (D) and basal (E) clays.

The <0.1 μm fraction is composed of smectite for samples D, 1, 2, 3 and 4, although small amounts of sepiolite can be detected in sample 2. Traces of illite are always present, but remained in significant amounts only in sample E, in which kaolinite is also observed. It is interesting to note the well-developed hydrated-smectite peak at 1.48 nm under air-dried conditions. This indicates that the presence of kerolite is not significant. Kerolite (k) or kerolite-stevensite (k-s) mixed-layers are characterized by the presence of non-expandable broad peaks at or near 1.0 nm (k) or expandable peaks at 1.3–1.2 expanding to 1.8–1.9 nm after glycolation (k-s, partially ordered), Brindley (1984); Martin de Vidales *et al.* (1988, 1991). However, Elton *et al.* (1997) showed an example of air-dried k-s type patterns that can be interpreted as a physical mixture of kerolite and stevensite under glycerol treatment.

Differences in smectite expandability are observed in the XRD patterns of the <0.1 μm fraction upon glycolation. The d_{001} basal spacings are located at 1.82 nm in samples 1 and 3 and at 1.72 nm in samples D, E, 2 and 4. The reflection at 1.82 nm is broader and shows a lower peak to background ratio than the 1.72 nm reflection. Large d_{001} spacings could indicate interstratification with kaolinite, but the second-order position (0.91 nm) is close to a regular order with respect to the 1.82 nm reflection. Moreover, in the case of smectite-kaolinite mixed-layer minerals, the 002 reflection shifts to lower spacings (Lanson and Bouchet, 1995). A simple deconvolution study was performed using the first and second orders of the basal spacing of the ethylene glycol-solvated <0.1 μm fraction. The shape of the deconvoluted peaks and their full-width at half height (FWHH) are shown in Figure 4. Both the 001 and 002 peaks can be deconvoluted into two bands: a lower-angle broad peak located at 1.82–1.84 (001)/0.89–0.92 (002) nm and a peak at 1.71–1.73 (001)/0.85–0.87 (002) nm. Using the Scherrer equation, the FWHH data yield 2–4 stacked layers for the lower angle reflections and 7–8 for the 1.7 nm reflection. The possible existence of anomalous positions due to the presence of very small bidimensional crystals has been outlined by Reynolds (1980) and Tettenhorst and Roberson (1973) and can be simulated using the Newmod2® computer program (Reynolds, 1985), considering the presence of very thin (2 layers thick) smectite crystallites. Figure 5 shows the simulated patterns. Consequently, the broad 001 reflection with a high low-angle shoulder in samples 1 and 3 is attributed to a reduction in the coherent scattering domain size.

The random powder diffraction patterns of the 060 region (from 59 to 62°2θ CuKα angular range) in the <0.1 μm and 2–1 μm fractions are shown in Figure 6. The main trioctahedral character of lacustrine clays is demonstrated, in both fractions, by the presence of the 0.1523–0.1530 nm reflection. The peak at 0.1502–0.1507 nm is attributed to a dioctahedral phase. The intensity of the 0.150 nm reflection is greater in the 2–1 μm fraction of the lacustrine clays, especially in sample 2. The reflection at 0.152 nm in the coarsest fraction of sample 2 might be attributed to an Fe-rich dioctahedral phase.

The transitional sample (D) pattern shows the presence of a trioctahedral mineral (0.153 nm) and a dioctahedral one (0.150 nm) both in the <0.1 μm and in the 2–1 μm samples. The coarsest fraction shows a 0.149 nm peak characteristic of kaolinite.

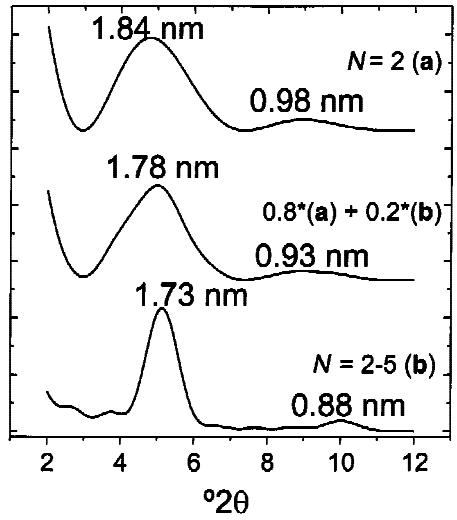

Figure 5. XRD patterns showing the first- and second-order basal reflections of ethylene glycol-solvated poorly crystallized smectites simulated using the Newmod2® computer program (Reynolds, 1985). *N*: number of coherently stacked smectite layers. (a) Two-layer smectite crystallites; (b) normal population of crystallites ranging from $N = 2$ to $N = 5$; a*0.8 + b*0.2: mixing of 80% of pattern a and 20% of pattern b.

https://doi.org/10.1346/CCMN.2003.0510413 Published online by Cambridge University Press

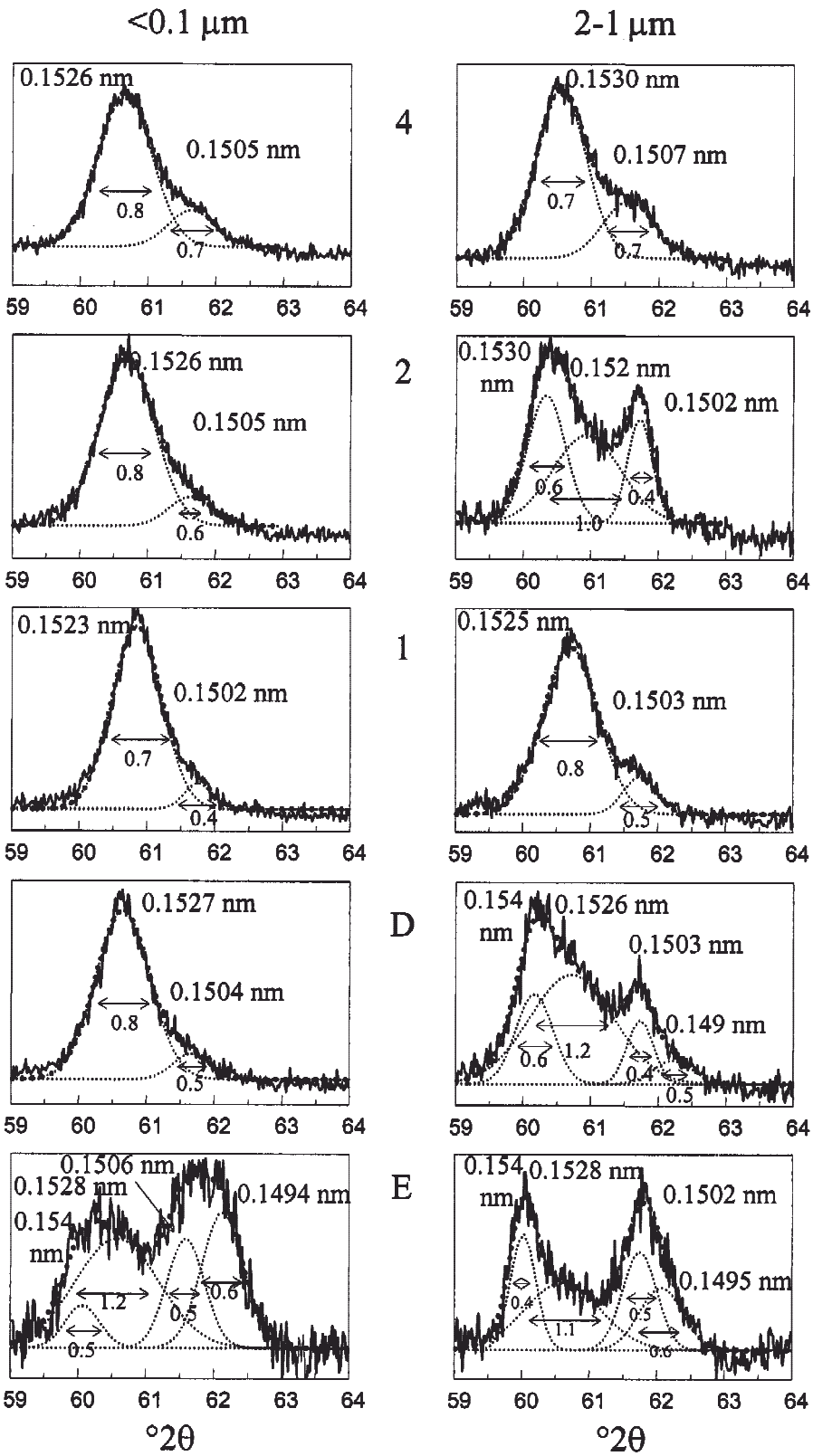

Figure 6. Random powder XRD patterns decomposition in the 060 region of the coarse (2 – 1 μm) and fine (<0.1 μm) fractions from the selected samples.

https://doi.org/10.1346/CCMN.2003.0510413 Published online by Cambridge University Press

A complex pattern in the 060 region is observed in <0.1 μm and 2–1 μm size-fractions of the basal clay (E) due to the presence of a trioctahedral phase (0.1528 nm) and dioctahedral (0.1502–0.1506 nm) 2:1 phases and kaolinite (0.149 nm). The 0.154 nm peak is attributed to the presence of quartz in significant amounts; this can also be observed in the 2–1 μm fraction of the D sample. This is more clearly shown in the random powder diffraction patterns of the 18–32°2θ angular range (Figure 7). The absence of non-phyllosilicate minerals in <0.1 μm fractions of samples D and 1 is also shown.

FTIR characterization and charge distribution

The OH-stretching region spectra of the <0.1 μm and 2–1 μm fractions of the six selected clays are compared in Figure 8. With regard to the fine fraction, both transitional (D) and lacustrine clays (1, 2, 3 and 4) show a well defined 3678 cm^{-1} band and a shoulder at 3714 cm^{-1}, both corresponding to the Mg_3OH vibration (Pelletier *et al.*, 1999). This confirms that the phyllosilicates are predominantly trioctahedral in lacustrine and transitional clays. A slight Al_2OH band at 3620 cm^{-1} is also present, especially in the 2, 4 and D samples, which is related to the presence of dioctahedral phases. The basal clay spectrum (E) shows the predominance of kaolinite (sharp intense bands near 3700 and 3620 cm^{-1} with sharp, less intense bands near 3675 and 3650 cm^{-1}) over a dioctahedral component (broad band centered near 3620 cm^{-1}).

The IR spectra of the coarse fraction in lacustrine samples also show the presence of tri- and dioctahedral phases. However, sample 1 is mainly composed of trioctahedral phases (Mg_3OH bands at 3678 cm^{-1} and 3698 cm^{-1}) while in sample 2 dioctahedral phases are dominant (broad 3620 cm^{-1} Al_2OH band). The transitional clay (D) coarse fraction shows a more complex FTIR spectrum, in accordance with the XRD analysis. The occurrence of kaolinite (described above) is clearly observed. An anomalously intense band (for kaolinite) at 3678 cm^{-1} results from the overlapping of a Mg_3OH component. Moreover, as in the finest fraction, another

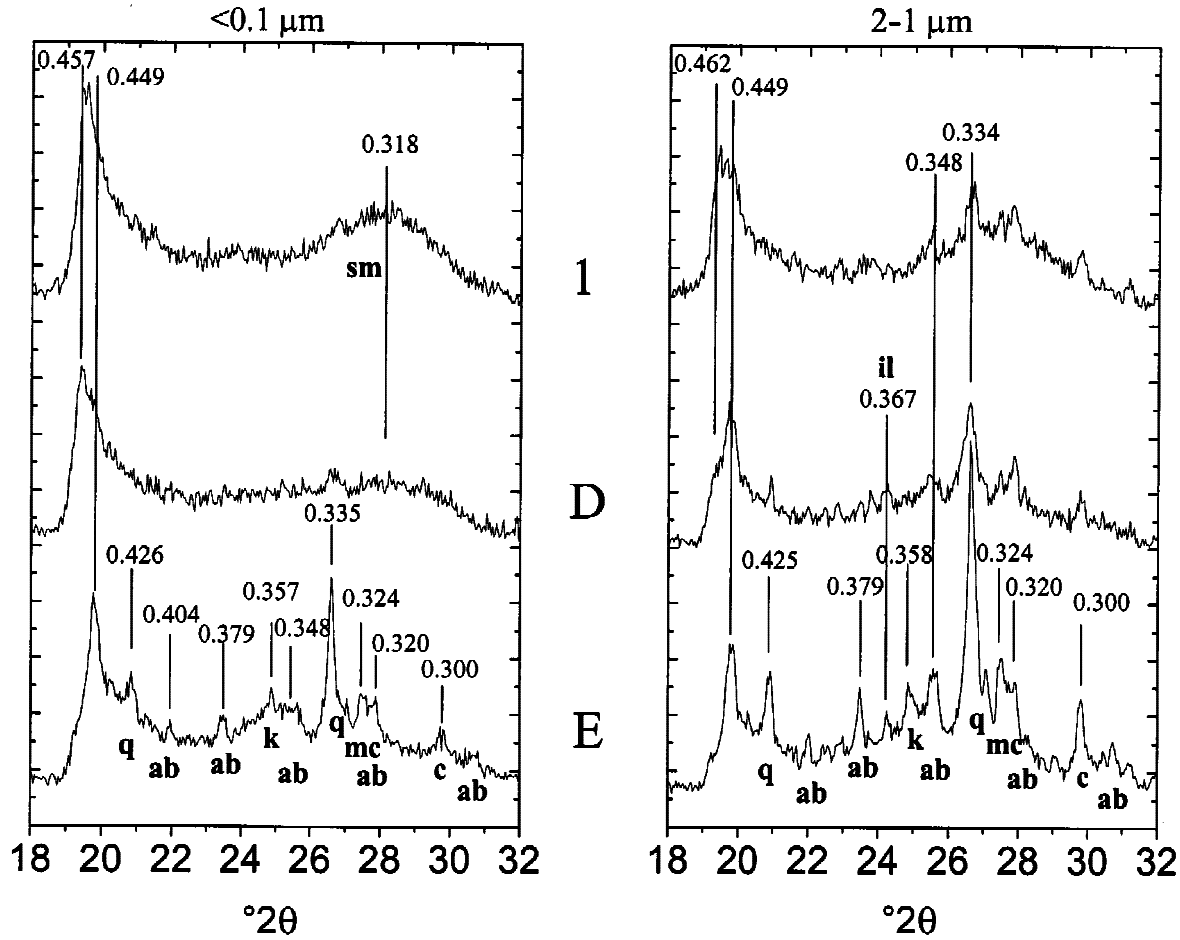

Figure 7. Random powder XRD patterns in the 18–32°2θ region of the coarse (2–1 μm) and fine (<0.1 μm) fractions from samples 1, E and D. q: quartz, ab: albite, mc: microcline, sm: smectite, il: illite, k: kaolinite, c: calcite. Peak values are in nm.

https://doi.org/10.1346/CCMN.2003.0510413 Published online by Cambridge University Press

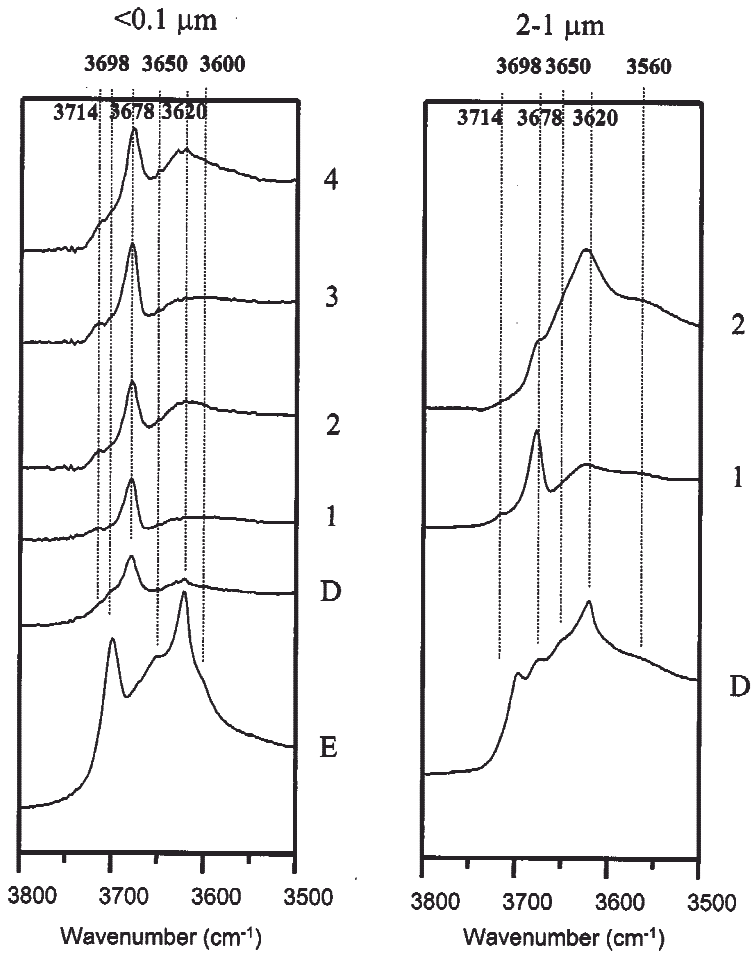

Figure 8. FTIR spectra in the OH-stretching region of the <0.1 μm fraction from selected samples and of the 2–1 μm fraction from several selected samples.

smectitic component centered near 3620 cm^{-1} also overlaps. The lower-frequency band located near 3560 cm^{-1}, which can also be identified in the coarse fraction of lacustrine clays (samples 1 and 2), is attributed to Fe(III)-rich 2:1 phyllosilicates (Russell, 1987).

The layer charge has been measured using the method proposed by Petit *et al.* (1998, 1999). According to this method, the normalized integrated intensity of the $\nu_4NH_4^+$ deformation band at 1400 cm^{-1} in IR spectra is proportional to the total charge or, in other words, to the CEC. Figure 9 shows the linear relationship found between the CEC determined by a chemical method and the normalized A_{NH_4} area in the <0.1 μm fraction of selected samples. Figure 10 shows the variation of the normalized integrated intensities of the NH_4^+ band before and after the Hofmann and Klemen treatment (1950). All of the samples show a decrease in the layer charge after lithium treatment. The higher the $A_{NH_4}/A_{NH_4\text{-}Li}$ ratio the more important the charge reduction. Samples 2, 4, D and E show the highest percentage of charge reduction

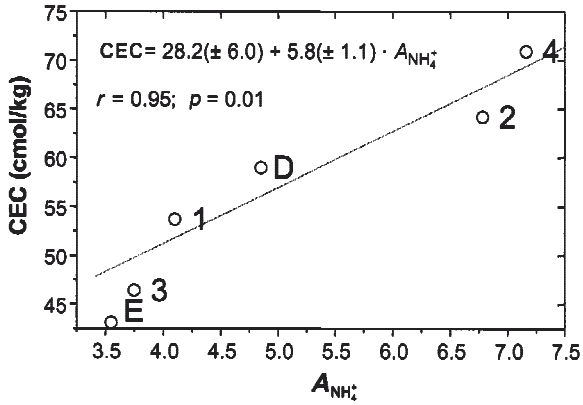

Figure 9. Relationship between the CEC determined by the Co(II) sulphate method (Rhodes and Brown, 1994) and the normalized integrated intensity of the $\nu_4 NH_4^+$ deformation band at 1400 cm^{-1} ($A_{NH_4^+}$) in the IR spectra of the <0.1 μm fraction of the selected samples.

https://doi.org/10.1346/CCMN.2003.0510413 Published online by Cambridge University Press

(~40%). In samples 1 and 3, the charge reduction is ~30%. The decrease in the layer charge arises from the migration of Li^+ to the octahedral vacancies.

In the case of stevensite ($Mg_2\square$), only one of the two vacancy-generated negative charges is counteracted: $(Mg2\square)^{2-} + Li^+ = (Mg2Li)^{1-}$. Then the % of octahedral charge should be obtained from the % of charge reduction multiplied by a factor of 2. Ideal Mg saponites of synthetic or hydrothemal origin ($(X^+_{x-y})(Mg_{6-y}R^{3+}_y)(Si_{8-x}Al_x)O_{20}(OH)_4$; *i.e.* Suquet *et al.* (1975, 1977)) do not show octahedral vacancies, and the presence of trivalent cations provides a slight positive charge to the octahedral sheet. Clearly, this is not the case for the documented saponites of sedimentary origin, Post (1984); Galán *et al.* (1986). The presence of R^{3+} (Al) and the cation deficiency respecting the trioctahedral sheet (sum of octahedral cations <6) allows AlMg□ vacancies to exist. Hence, the octahedral charge can be completely reduced in these sites. This means that the percentage of octahedral charge cannot be determined precisely in saponite-stevensite mixtures.

Nevertheless, the presence of vacancies in the octahedral sheet confirms the predominance of stevensite in samples 1 and 3, mainly composed of a Mg trioctahedral phyllosillicate with minor amounts of a dioctahedral phase (XRD, Figure 6, sample 1). The presence of saponite cannot be excluded from samples 2 and 4 either. However, discrete dioctahedral domains are significant (XRD, Figure 6 and FTIR, Figure 8). This means that AlMg□ vacancies linked to trioctahedral domains cannot fully explain the important octahedral charge reduction. Thus, stevensite is also present in these samples.

Chemical composition trends

The average chemical composition obtained by EDS-SEM in different size-fractions of selected samples was expressed as atomic distribution on a 2:1 phyllosilicate unit-cell structural basis (44 negative charges) in Table 4. Calculations were performed assuming Fe(III) given to the presence of Fe(III)-rich phases detected in the FTIR characterization. Moreover, Cuevas *et al.* (1993) demonstrated the predominance of Fe(III) in the <0.5 μm size-fractions of Mg trioctahedral smectites in the Madrid Basin.

The atomic distribution in the <0.5 μm fraction from EDS data (Table 4) showed a systematically lower Mg content than in the XRF analyses (Table 3) due to the

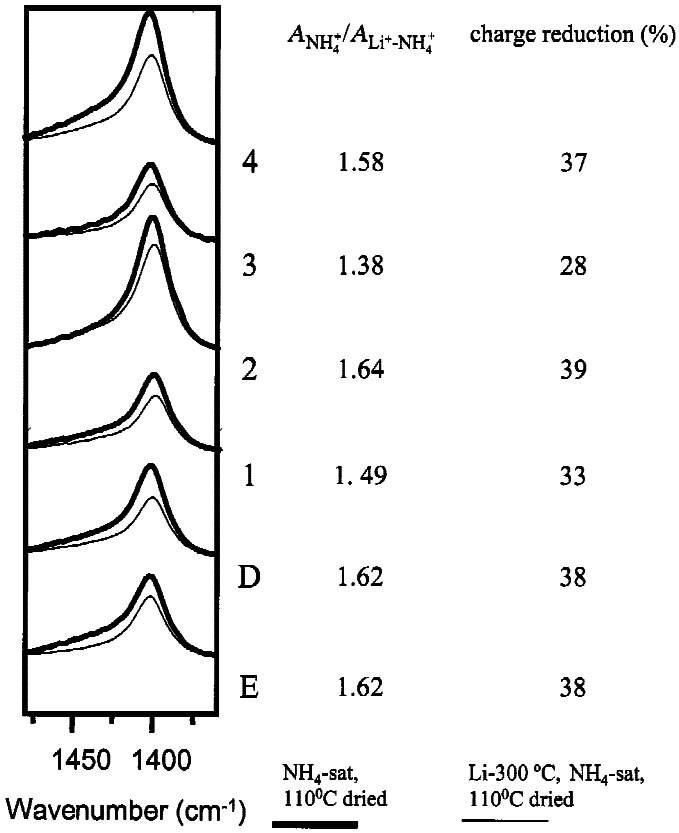

Figure 10. ν_4 NH_4^+ deformation band at 1400 cm^{-1} in the IR spectra before (thick line) and after (thin line) the Hofmann-Klemen treatment (1950), normalized intensity ratio $A_{NH_4^+}/A_{Li\text{-}NH_4^+}$, and the percentage of charge reduction for the <0.1 μm fraction of the selected samples.

https://doi.org/10.1346/CCMN.2003.0510413 Published online by Cambridge University Press

Table 4. Atomic distribution in a 2:1 phyllosilicate unit-cell ($O_{20}(OH)_4$ basis) calculated from the chemical analyses determined by SEM-EDX in the 5 to <0.5 μm size range. Standard deviations in parenthises (δ).

Sample	E				D			
Fraction	5–2 μm	2–1 μm	1–0.5 μm	<0.5 μm	5–2 μm	2–1 μm	1–0.5 μm	<0.5 μm
Si^{IV} (δ)	6.23 (0.43)	6.53 (0.25)	6.32 (0.04)	6.51 (0.06)	6.69 (0.26)	6.73 (0.20)	6.80 (0.02)	7.02 (0.05)
Al^{IV} (δ)	1.77 (0.04)	1.47 (0.21)	1.68 (0.04)	1.49 (0.06)	1.31 (0.29)	1.27 (0.13)	1.20 (0.01)	0.98 (0.02)
Al^{VI} (δ)	2.34 (0.04)	2.73 (0.43)	2.49 (0.08)	2.45 (0.07)	1.50 (0.32)	1.75 (0.13)	1.15 (0.01)	0.82 (0.01)
Mg^{VI} (δ)	0.68 (0.07)	0.57 (0.09)	0.73 (0.03)	0.88 (0.01)	2.41 (0.13)	2.31 (0.30)	2.98 (0.08)	3.55 (0.01)
Fe^{3+VI} (δ)	1.24 (0.07)	0.84 (0.32)	1.02 (0.05)	0.95 (0.09)	0.86 (0.29)	0.65 (0.04)	0.77 (0.03)	0.68 (0.01)
Ti^{VI} (δ)	0.07 (0.05)	0.06 (0.04)	0.08 (0.02)	0.07 (0.00)	0.05 (0.02)	0.06 (0.02)	0.08 (0.02)	0.06 (0.00)
SOC[1]	4.33 (0.05)	4.20 (0.01)	4.32 (0.02)	4.35 (0.04)	4.82 (0.10)	4.78 (0.36)	4.98 (0.06)	5.11 (0.05)
Ca^{2+} (δ)	0.03 (0.03)	0.03 (0.01)	0.02 (0.00)	0.04 (0.00)	0.15 (0.04)	0.09 (0.03)	0.15 (0.01)	0.33 (0.01)
Mg^{2+} (δ)[2]	0.15 (0.03)	0.11 (0.10)	0.14 (0.00)	0.19 (0.01)	0.09 (0.11)	0.12 (0.02)	0.11 (0.06)	–
K^+ (δ)	1.03 (0.11)	1.10 (0.38)	1.05 (0.01)	0.79 (0.05)	0.73 (0.10)	0.76 (0.10)	0.64 (0.00)	0.48 (0.01)

Sample	1				2			
Fraction	5–2 μm	2–1 μm	1–0.5 μm	<0.5 μm	5–2 μm	2–1 μm	1–0.5 μm	<0.5 μm
Si^{IV} (δ)	7.47 (0.41)	7.62 (0.38)	7.78 (0.11)	8.00 (0.00)	6.35 (0.55)	6.60 (0.38)	6.60 (0.11)	7.33 (0.05)
Al^{IV} (δ)	0.53 (0.17)	0.38 (0.06)	0.22 (0.02)	–	1.65 (0.15)	1.40 (0.18)	1.40 (0.13)	0.67 (0.04)
Al^{VI} (δ)	1.28 (0.02)	1.27 (0.01)	0.57 (0.08)	0.55 (0.04)	2.10 (0.36)	1.97 (0.18)	1.58 (0.05)	0.86 (0.03)
Mg^{VI} (δ)	3.07 (0.03)	2.95 (0.07)	3.64 (0.09)	4.39 (0.05)	1.39 (0.35)	1.49 (0.31)	1.58 (0.09)	3.56 (0.01)
Fe^{3+VI} (δ)	0.37 (0.08)	0.44 (0.03)	0.67 (0.14)	0.22 (0.01)	0.78 (0.07)	0.82 (0.07)	1.10 (0.11)	0.57 (0.03)
Ti^{VI} (δ)	0.05 (0.01)	0.05 (0.02)	0.05 (0.02)	0.02 (0.00)	0.12 (0.00)	0.14 (0.00)	0.16 (0.02)	0.05 (0.01)
SOC[1]	4.77 (0.07)	4.71 (0.02)	4.93 (0.00)	5.16 (0.07)	4.39 (0.06)	4.42 (0.06)	4.42 (0.01)	5.04 (0.04)
Ca^{2+} (δ)	0.08 (0.02)	0.02 (0.01)	0.06 (0.01)	0.04 (0.03)	0.02 (0.01)	0.03 (0.01)	0.03 (0.01)	0.05 (0.04)
Mg^{2+} (δ)[2]	0.19 (0.05)	0.23 (0.05)	0.26 (0.05)	0.35 (0.08)	0.01 (0.01)	0.11 (0.01)	0.06 (0.02)	0.25 (0.02)
K^+ (δ)	0.70 (0.12)	0.65 (0.04)	0.38 (0.00)	0.11 (0.00)	1.69 (0.06)	1.21 (0.06)	1.38 (0.08)	0.46 (0.02)

Sample	3				4			
Fraction	5–2 μm	2–1 μm	1–0.5 μm	<0.5 μm	5–2 μm	2–1 μm	1–0.5 μm	<0.5 μm
Si^{IV} (δ)	7.62 (0.40)	7.78 (0.43)	7.83 (0.06)	7.96 (0.03)	7.23 (0.20)	7.37 (0.11)	7.32 (0.05)	7.47 (0.03)
Al^{IV} (δ)	0.38 (0.05)	0.22 (0.42)	0.17 (0.05)	0.04 (0.02)	0.77 (0.03)	0.63 (0.03)	0.68 (0.05)	0.53 (0.01)
Al^{VI} (δ)	1.36 (0.02)	0.62 (0.12)	0.57 (0.04)	0.46 (0.04)	1.95 (0.19)	1.14 (0.06)	1.09 (0.06)	0.79 (0.01)
Mg^{VI} (δ)	3.13 (0.56)	4.20 (0.40)	4.51 (0.01)	4.80 (0.02)	2.28 (0.26)	3.37 (0.21)	3.55 (0.08)	4.20 (0.04)
Fe^{3+VI} (δ)	0.24 (0.10)	0.30 (0.31)	0.16 (0.00)	0.07 (0.01)	0.35 (0.02)	0.34 (0.04)	0.38 (0.06)	0.27 (0.03)
Ti^{VI} (δ)	0.05 (0.14)	0.04 (0.01)	0.03 (0.00)	0.01 (0.00)	0.05 (0.01)	0.11 (0.02)	0.03 (0.00)	0.01 (0.00)
SOC[1]	4.78 (0.31)	5.16 (0.05)	5.27 (0.05)	5.34 (0.05)	4.63 (0.10)	4.96 (0.09)	5.05 (0.08)	5.27 (0.06)
Ca^{2+} (δ)	0.13 (0.01)	0.14 (0.00)	0.17 (0.00)	0.20 (0.01)	0.15 (0.04)	0.17 (0.01)	0.24 (0.02)	0.25 (0.02)
Mg^{2+} (δ)[2]	0.16 (0.14)	0.22 (0.07)	0.20 (0.08)	0.19 (0.07)	0.11 (0.10)	0.13 (0.06)	0.08 (0.09)	0.11 (0.09)
K^+ (δ)	0.54 (0.42)	0.18 (0.02)	0.10 (0.02)	0.03 (0.00)	0.59 (0.03)	0.41 (0.07)	0.41 (0.03)	0.19 (0.01)

[1] SOC: sum of octahedral cations

[2] Exchangeable Mg has been estimated assuming a linear relationship between exchangeable cation occupation and K^+ content, trending to zero as K^+ occupation approaches 1.8 (typical illite) and setting the total X^+ at $K^+ = 0$ value to that of the <0.5 μm Ca-homoionized fraction (Table 3).

low atomic weight of Mg. This has a minor influence on comparisons of the chemical composition of the different fractions.

The atomic distribution in a 2:1 phyllosilicate unit-cell are plotted to evaluate the chemical evolution of the samples. The relationship between K^+ and Si^{4+} is shown in Figure 11. The chemical composition of samples ranges from micaceous (high K^+ occupancy) in basal clay (E) to ideal smectite compositions in lacustrine clays (1, 3, 4 and <0.5 μm fraction of sample 2). Chemical differences with size-fraction are observed in all the samples, especially in sample 2. Finer fractions show an increase of tetrahedral Si^{4+} and, consequently, a decrease in the layer charge.

The composition of the octahedral sheet and the value of the tetrahedral charge are represented in Figure 12 to elucidate the nature of smectite which represents the product of the evolution of the parent materials. There is a straight line defining the uptake of Mg^{2+} from basal to lacustrine clays and from the coarser to finer fraction. The ideal stevensitic compositions predominate in the lacustrine clays: in samples 1, 3 and 4, even for some single point analyses from platelets in coarse fractions and in the <0.5 μm fraction of sample 2. The transitional sample (D) shows a mixing trend from the dioctahedral to Mg trioctahedral smectites. This is illustrated by the progressive increase in Mg^{2+} content in the two coarser fractions. The sum of octahedral cations (5–5.3) also

https://doi.org/10.1346/CCMN.2003.0510413 Published online by Cambridge University Press

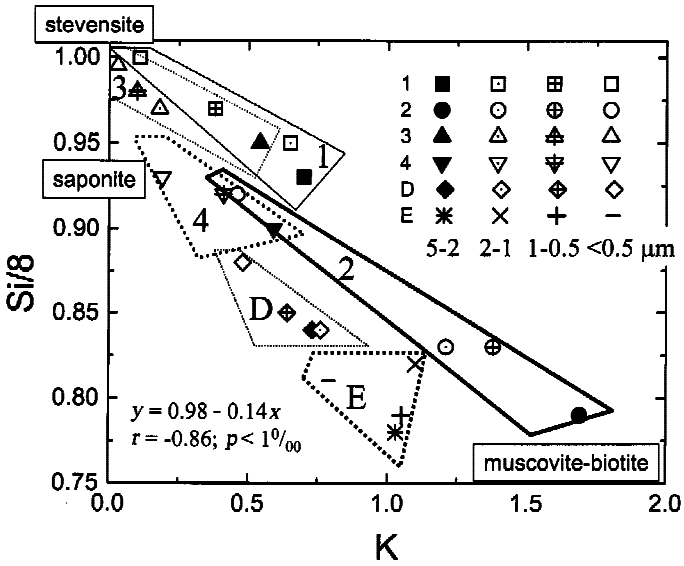

Figure 11. Relationship between K and tetrahedral Si distribution in a 2:1 phyllosilicate on unit-cell structural bases, from chemical analysis by EDX-SEM in the different size-fractions of the selected samples.

confirm the physical mixture between the di- and trioctahedral phases.

The relative Fe proportion in octahedral sites decreases linearly as tetrahedral Si increases with mineral evolution (Figure 13). The regression line can be extrapolated from the basal clay (E) platelets, which are fully composed of an Fe-rich, micaceous assemblage towards the Mg-rich smaller size-fractions of lacustrine clays. This could indicate that trioctahedral micas (biotite) were present, in addition to Al dioctahedral phyllosilicates such as kaolinite, illite or even smectite, in previous stages of alteration or in the parent material of the sediment. This is consistent with the presence of Fe-rich minerals as components of the multiphase mixture characterizing the coarser fractions of basal and transitional clays, according to XRD and FTIR data.

DISCUSSION

Magnesium uptake by clay weathering products or suspended colloids has been claimed to be the main process that involves Mg aluminosilicate authigenesis in

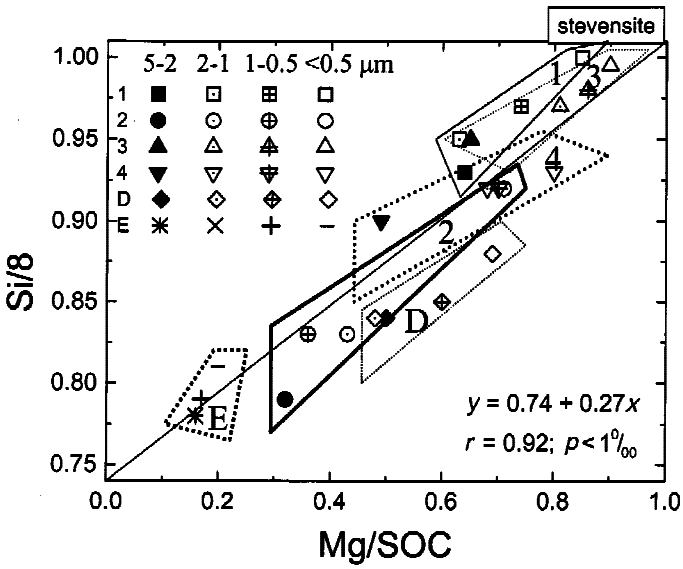

Figure 12. Relationship between Mg (Mg and sum of octahedral cation (SOC) ratio) and tetrahedral Si in a 2:1 phyllosilicate unit-cell, from chemical analysis by EDX-SEM in the different size-fractions of the selected samples.

https://doi.org/10.1346/CCMN.2003.0510413 Published online by Cambridge University Press

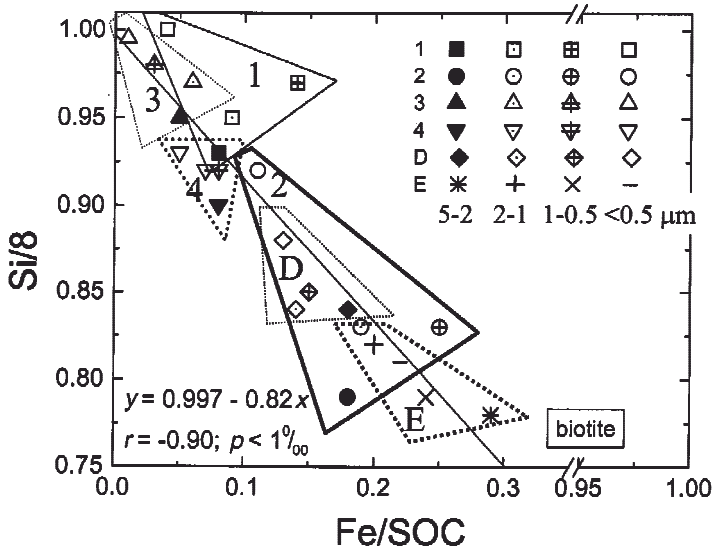

Figure 13. Relationship between Fe (Fe and SOC ratio) and tetrahedral Si distribution in a 2:1 phyllosilicate on unit-cell structural bases, from chemical analysis by EDX-SEM in the different size-fractions of the selected samples.

saline-lake systems (Wollast *et al.* 1968; Jones and Weir, 1983). Banfield *et al.* (1991) showed by TEM-AEM that the Mg smectite formation is a topotactic overgrowth reaction in which a pure Mg silicate phase of stevensitic composition is formed. The present paper can be added to verify these ideas since XRD and FTIR data clearly show the significant stevensitic nature of the Mg clays.

The source of colloids that acted as stevensite templates was investigated. The finer size-fractions of the basal clay showed a complex mineralogy and chemistry that includes trioctahedral, dioctahedral and intermediate Fe-Mg-rich compositions of altered mica-type minerals. Coarser fractions of the transitional clays showed similar features, also found in coarse lacustrine clay fractions. This type of debris has fed the initial constrained lacustrine basin.

The composition of coarser fractions in basal clay (5–1 μm particles) can be seen as typical of oxidizing weathering processes in which some Fe^{3+} is ejected from the octahedral sheet in the alteration of granite biotites (Gilkes *et al.*, 1972). These compositions confirm the existence of a complex mixture of minerals in which Fe,Mg-rich and Al-rich phases can be physically mixed as indicated by XRD and FTIR data. Biotite can be oxidized yielding some Fe-rich dioctahedral and tri-octahedral alteration by-products (Fordham, 1990a, 1990b). According to Fordham (1990b), the analyses quoted here seem to fit more closely a dioctahedral K-rich vermiculite (SOC 4.22, 1.49 total Fe), with all the Mg in the octahedral sheet.

Maintenance of the same minerals across the size-fractions in the basal sediments is a direct consequence of their sedimentation rate, more rapid than the subsequent sediments (Leguey *et al.*, 1995). The lower the sedimentation rate, the higher the precipitation and growth of stevensitic material, and the more dilution and alteration of pre-existent phyllosilicates.

The nature of the saponitic clays, depending on the average chemical data has been clarified. These materials are mainly mixtures of saponite, stevensite and several dioctahedral phases. Some of the dioctahedral phases involved have a non-negligible Mg content (*i.e.* chemical analysis of the 5–1 μm of transitional clay sample D in Table 2). This is part of the explanation for the resulting saponitic formula. The origin is probably the diagenetic alteration of oxidized biotite, present in the coarser fractions. This is supported by clean laminae of biotite flakes seen on fine-grained greenish sands that often lie intercalated in closely related Miocene intermediate-unit deposits (Hoyos *et al.*, 1985). The presence of some trioctahedral component in the coarse fractions analyzed can be deduced from XRD, but its nature was not clearly established.

CONCLUSIONS

The chemical and structural properties of Mg smectites in the Vicálvaro sepiolite deposit have been studied in detail. The XRD and FTIR data demonstrate that they are a multiphase mixture in which dioctahedral and trioctahedral minerals are separate phases. The materials currently referred to as Mg smectites in the lacustrine strata of the Neogene Madrid Basin are composed of a complex mixture of stevensite, saponite and mica-type minerals. Although the presence or absence of saponite cannot be confirmed absoutely, the stevensite is a significant component of these Mg smectites. This fact is proven by the calculated layer charge reduction after the Hofmann-Klemen effect (1950), which established the predominance of an

https://doi.org/10.1346/CCMN.2003.0510413 Published online by Cambridge University Press

octahedral charge in these materials. Finally, micaceous minerals are important phases in the complex mixture. This is based on the increase in K and Al contents from the fine clay fractions to the coarse clay fractions, and on the chemical, XRD and IR evidence for the presence of ferric micaceous minerals.

ACKNOWLEDGMENTS

The authors would like to express their gratitude to E. Galán and B.F. Jones for their valuable comments and help in preparing the final manuscript.

REFERENCES

Ames, L.L. Jr., Sand, L.B. and Goldrich, S.S. (1958) A contribution on the Hector, California, bentonite deposit. *Economic Geology*, **53**, 22–37.

Banfield, J.F., Jones, B.F. and Veblen, D.R. (1991) An AEM-TEM study of weathering and diagenesis, Albert lake, Oregon: II. Diagenetic modification of the sedimentary assemblage. *Geochimica et Cosmochimica Acta*, **55**, 2795–2810.

Brindley, G.W. (1984) Order-disorder in clay mineral structures. Pp. 125–196 in: *Crystal Structures of Clay Minerals and their X-ray Identification* (G.W. Brindley and G. Brown, editors). Monograph **5**, Mineralogical Society, London.

Brunauer, S., Emmett, P.H. and Teller, E. (1938) Adsorption of gases in multimolecular layers. *Journal of the American Chemical Society*, **60**, 309–319.

Cuevas, J., Pelayo, M., Rivas, P. and Leguey, S. (1993) Characterization of Mg-clays from the Neogene of the Madrid Basin and their potential as backfilling and sealing material in high level radioactive waste disposal. *Applied Clay Science*, **7**, 383–406.

Cuevas, J., Medina, J.A., Casas, J., Martin-Rubi, A., Torres, S., Alvarez, A. and Leguey, S. (1995) Heulandita asociada a esmectitas-Mg en el yacimiento de sepiolita de Vicalvaro. (Cuenca Neogena de Madrid). *Boletin de la Sociedad Española de Mineralogia*, **18**, 143–155.

Darragi, F. and Tardy, Y. (1987) Authigenic trioctahedral smectites controlling pH, alkalinity, silica and Mg-concentrations in alkaline lakes. *Chemical Geology*, **63**, 59–72.

De Santiago, C., Suarez, M., Garcia, E. and Doval, M. (2000) Mg-rich smectite "precursor" phase in the Tagus Basin, Spain. *Clays and Clay Minerals*, **48**, 366–373.

Elton, N.J., Hooper, J.J. and Holyer, V.A.D. (1997) An occurrence of stevensite and kerolite in the Devonian Crousa gabbro at Dean Quarry, The Lizard, Cornwall, England. *Clay Minerals*, **32**, 241–252.

Fordham, A.W. (1990a) Formation of trioctahedral illite from biotite in a soil profile over granite gneiss. *Clays and Clay Minerals*, **38**, 187–195.

Fordham, A.W. (1990b) Weathering of biotite into dioctahedral clay minerals. *Clay Minerals*, **25**, 51–63.

Galán, E., Alvarez, A. and Esteban, M.A. (1986) Characterization and technical properties of a Mg-rich bentonite. *Applied Clay Science*, **1**, 295–309.

Gilkes, R.J., Young, R.C. and Quirk, J.P. (1972) The oxidation of octahedral iron in biotite. *Clays and Clay Minerals*, **20**, 303–315.

Hay, R.L., Gudman, S.G., Matthews, J.C., Lander, R.H., Duffin, M.E. and Kyser, T.K. (1991) Clay mineral diagenesis in Core KH-3 of Searles Lake, California. *Clays and Clay Minerals*, **39**, 84–96.

Hofmann, U. and Klemen, E. (1950) Loss of exchangeability of lithium ions in bentonite on heating. *Zeitschrift für Anorganische und Allgemeine Chemie*, **262**, 95–99.

Hoyos, M., Junco, F., Plaza, J.M., Ramirez, A. and Ruiz Sanchez-Porro, J. (1985) El mioceno de Madrid. Pp. 9–16 in: *Geologia y paleontologia del terciario continental de la provincia de Madrid*. Consejo Superior de Investigaciones Cientificas, Museo de Ciencias Naturales, Madrid.

Jones, B.F. (1986) Clay mineral diagenesis in lacustrine sediments. *US Geological Survey Bulletin*, **1578**, 291–300.

Jones, B.F. and Galán, E. (1988) Sepiolite and palygorskite. Pp. 631–674 in: *Hydrous Phyllosilicates (Exclusive of Micas)* (S.W. Bailey, editor). Reviews in Mineralogy, **19**, Mineralogical Society of America, Washington D.C.

Jones, B.F. and Weir, A.H. (1983) Clay minerals of Lake Albert, an alkaline saline lake. *Clays and Clay Minerals*, **31**, 161–172.

Khoury, H.H., Eberl, D.D. and Jones, B.F. (1982) Origin of magnesium clays from the Amargosa desert, Nevada. *Clays and Clay Minerals*, **30**, 327–336.

Lanson, B. and Bouchet, A. (1995) X-ray diffraction identification of clay minerals. Pp. 90–115 in: *Structure et transformation des argiles dans les champs petroliers et geothermiques: improvements induced by numerical data*. ELF Aquitaine production **19**, Pau, France.

Leguey, S., Martin-Rubi, J.A., Casas, J., Marta, J., Cuevas, J., Alvarez, A. and Medina, J.A. (1995) Diagenetic evolution and mineral fabric in sepiolitic materials from the Vicalvaro deposit (Madrid Basin). Pp. 383–392 in: *Clays Controlling the Environment* (G.J. Churchman, R.W. Fitzpatrick and R.A. Eggleton, editors). Proceedings of the 10th International Clay Conference, Adelaide, Australia, 1993. CSIRO Publishing, Melbourne, Australia.

Martin de Vidales, J.L., Pozo, M., Medina, J.M. and Leguey, S. (1988) Formacion de sepiolita-paligorskita en litofacies lutitico-carbonaticas en el sector de Borox-Esquivias (cuenca de Madrid). *Estudios Geologicos*, **44**, 7–18.

Martin de Vidales, J.L., Pozo, M., Alia, J.M., Garcia-Navarro, F. and Rull, F. (1991) Kerolite-stevensite mixed-layers from the Madrid Basin, Central Spain. *Clay Minerals*, **26** 329–342.

Ordoñez, S., Calvo, J.P., Garcia del Cura, M.A., Alonso Zarza, A.M. and Hoyos, M. (1991) Sedimentology of sodium sulphate and special clays from the Tertiary Madrid Basin (Spain). *Specical Publication of the International Association of Sedimentology*, **13**, 1217–1229.

Pelletier, M., Michot, L.J., Barrès, O., Humbert, B., Petit, S. and Robert, J.L. (1999) Influence of KBr conditioning on the IR hydroxyl-stretching region of saponites. *Clay Minerals*, **34**, 439–445.

Petit, S., Prot, T., Decarreau, A., Mosser, C. and Toledo-Groke, M.C. (1992) Crystallochemical study of a population of particles in smectites from a lateritic weathering profile. *Clays and Clay Minerals*, **40**, 436–445.

Petit, S., Righi, D., Madejová, J. and Decarreau, A. (1998) Layer charge estimation of smectites using infrared spectroscopy. *Clay Minerals*, **33**, 579–591.

Petit, S., Righi, D., Madejová, J. and Decarreau, A. (1999) Interpretation of the infrared NH_4^+ spectrum of the NH_4^+-clays: application to the evaluation of the layer charge. *Clay Minerals*, **34**, 543–549.

Post, J.L. (1984) Saponite from near Ballarat, California. *Clays and Clay Minerals*, **32**, 147–153.

Ramirez, S., Garralon, A., Cuevas, J., Martin-Rubi, J.A., Casas, J., Alvarez, A. and Leguey, S. (1996) Caracteristicas quimicas y propiedades de superficie en secuencias-tipo de materiales esmecticos en el yacimiento de sepiolita de Vicalvaro (Madrid). *Boletin de la Sociedad Española de Mineralogia*, **19**, 53–70.

Reynolds, R.C., Jr. (1980) Interstratified clay minerals. Pp. 249–304 in: *Crystal Structures of Clay Minerals and their*

X-ray Identification (G.W. Brindley and G. Brown, editors). Monograph **5**, Mineralogical Society, London.

Reynolds, R.C., Jr. (1985) *NEWMOD©* a computer program for the calculation of one-dimensional diffraction patterns of mixed-layer clays. Published by the author, R.C. Reynolds Jr., 8 Brook Dr., Hanover, New Hampshire, USA.

Rhodes, C.N. and Brown, D.R. (1994) Rapid determination of the cation exchange capacity of clays using Co(II). *Clays and Clay Minerals*, **29**, 799–801.

Russell, J.D. (1987) Infrared methods. Pp. 133–173 in: *A Handbook of Determinative Methods in Clay Mineralogy* (M.J. Wilson, editor). Blackie, Glasgow and London.

Suquet, H., de la Calle, C. and Pezerat, H. (1975) Swelling and structural organization of saponite. *Clays and Clay Minerals*, **23**, 1–9

Suquet, H., Iiyama, J.T., Kodama, H. and Pezerat, H. (1977) Synthesis and swelling properties of saponites with increasing layer charge. *Clays and Clay Minerals*, **25**, 231–242.

Tettenhorst, R. and Roberson, H.E. (1973) X-ray diffraction aspects of montmorillonites. *American Mineralogist*, **58**, 73–80.

Vali, H., Martin, R.F., Amarantidis, G. and Morteani, G. (1993) Smectite group minerals in deep sea sediments: Monomineralic solutions or multiphase mixtures? *American Mineralogist*, **78**, 127–129.

Wollast, R., Mackenzie, F.T. and Bricker, O.P. (1968): Experimental precipitation and genesis of sepiolite at earth-surface conditions. *American Mineralogist*, **53**, 1645–1662.

(*Received 4 July 2002; revised 24 February 2003; Ms. 674; A.E. Warren D. Huff*)